Investigations on the Output System of 300-GHz Gyrotrons

Debasish Mondal, *Graduate Student Member, IEEE*, S. Yuvaraj, *Member, IEEE*, Meenakshi Rawat, *Member, IEEE*, Manfred Thumm, *Life Fellow, IEEE*, and M. V. Kartikeyan, *Fellow, IEEE*

***Abstract*— This article presents the comprehensive design studies of the output systems consisting of nonlinear taper (NLT), quasi-optical launcher (QOL), RF window, and matching optics unit (MOU) for gyrotrons operating at 0.5 and 1 MW, respectively, for their potential application in the DEMOnstration tokamak. Two distinct designs of NLTs and QOLs are considered for these gyrotrons, along with the common design of RF window and MOU. The NLTs are optimized using our in-house code gyrotron design suite (GDS-2018). The transmission efficiency achieved for the NLT design of the 0.5 MW gyrotron is 99.48% and the 1 MW gyrotron is 99.53%. The initial design studies of dimpled wall QOLs are carried out using GDS-2018 and optimized through the commercial code launcher optimization tool (LOT). The QOL design for the 0.5 MW gyrotron contains 99.32% Gaussian content factor (GCF) in the output beam, while the QOL design for the 1 MW gyrotron contains 99.58% GCF. A single-disk RF window (made of chemically vapor deposited (CVD) diamond) and MOUs are designed using GDS-2018. The RF window separates the very low-pressure vacuum environment of the gyrotron from the external environment. MOU with two beam-shaping mirrors couples the synthetic Gaussian beam (SGB) to the corrugated waveguide, rectifying the off-axis incidence of the Gaussian beam while reducing beam astigmatism.**

I. Introduction

NUCLEAR fusion is a nonpolluting and efficient technology for future power generation that requires extremely high-power sources to achieve temperatures in the hundreds of millions of Kelvin. Gyrotrons are capable of delivering continuous waves (CWs) power ranging from kilowatts to megawatts. They are widely used in fusion research for electron cyclotron resonance heating (ECRH), plasma startup, and plasma stability control. Other prospective uses include industrial-scientific-medical applications, DNP-NMR spectroscopy in biomedical applications, the creation of soft X-rays, active denial systems for defense applications, and materials (glass, ceramic) processing [1], [2], [3], [4].

Recent advances in tokamaks, such as TEXTOR, ITER, and W7-X stellarator, employ conventional cavity gyrotrons, which were developed by several research organizations [3], [4], [5], [6]. The preliminary design and testing of the high-power gyrotrons at several controlled fusion (CF) reactors have validated their ECRH heating capacity [2], [3], [4]. Recently, a commercial prototype of the fusion reactor (DEMOnstration tokamak) is under development as a successor to the ITER tokamak with a larger core volume to process more fusion reactions and maximize the energy generation [7], [8], [9]. According to the EU-DEMO1-2015 baseline and preliminary conceptual studies, the gyrotrons in the DEMO tokamak should be operated at higher frequency regimes and higher power levels to maintain the large plasma volume [7], [9], [10], [11], [12]. Therefore, the conceptual design of the output system of the DEMO gyrotron plays a crucial role in achieving the desired high output power.

The complete gyrotron output system combines nonlinear taper (NLT), quasi-optical launcher (QOL), RF window, and matching optics unit (MOU). The NLT serves as a transformer, connecting the gyrotron's interaction cavity to the oversized input of the QOL. The dimpled wall QOL converts higher order modes to a Gaussian-like mode. An RF window, which separates the high pressure vacuum inside the gyrotron from the outer environment, allows the RF beam to exit the gyrotron. The MOU corrects beam ellipticity and reduces astigmatism. The output system with different sub-assemblies has been designed by our group for various gyrotron designs [13], [14], [15]. The comparison of analytic results with the numerical results of a Vlasov launcher that converts the waveguide mode to a nearly Gaussian-like beam

has been reported in [16]. Notably, a QOL with 90% of Gaussian-mode content and 95% of the RF window transmission efficiency has been reported for multifrequency operation of a gyrotron in [17]. A feasible analysis of 236-GHz conventional cavity DEMO gyrotron has been reported in [18], whereas, the preprototype design of different subcomponents of the DEMO gyrotron output system has been manufactured and tested by [19]. Further, the feasibility of manufacturing a 1.3 mm thick, unpolished diamond Brewster-angle window for the DEMO fusion reactor has been assessed in [20]. The wave phase reconstruction computation has been performed on different planes at varied distances from the launcher using iterative phase retrieval algorithm (IPRA) in [15], [21], and [22]. Furthermore, an MOU has been designed to couple the RF beam to a 50-mm waveguide for ITER Tokamak in [23] and to a 63.5-mm waveguide in [24].

The current study focuses on designing and optimizing output systems of two 300-GHz gyrotrons with the output power level of 0.5 and 1 MW, respectively. The operating cavity modes are $TE_{41,12}$ (0.5 MW) and $TE_{49,18}$ (1 MW), respectively, for the corresponding power levels [10], [11]. The purpose of designing 0.5 and 1 MW gyrotrons is to offer flexibility for different plasma heating needs in advanced tokamak reactors such as DEMO. The 0.5 MW gyrotrons cater to scenarios where a lower power output is sufficient, while the 1 MW gyrotrons are designed to provide higher power when needed. This flexibility allows for optimal power utilization, minimizes the number of gyrotrons required for operation, and simplifies maintenance demands. The study encompasses the design investigation of the MOU, aimed at efficiently transporting the Gaussian-like beam from the gyrotron's output window to the tokamak core. A detailed analysis of common mirror profiles within the MOU, comprising two beam-shaping mirrors forming an external mirror system strategically placed after the RF window, ensures efficient coupling of the output beam to the corrugated waveguide while preserving beam ellipticity. The investigation comprises numerous numerical experiments using a synthetic Gaussian beam (SGB) post the RF window's output plane. These numerical experiments estimate ellipticity and astigmatism, crucial for optimizing the MOU design. This unique methodology, a highlight of this work, facilitates a simple yet accurate estimation of the MOU design. The precision in design ensures high-power performance, and the comprehensive approach, including IPRA for mirror profile generation, emphasizes the significance for potential application in the DEMO tokamak.

In summary, the novelty of the work lies in the design studies of common RF window and MOU for both the power levels of 0.5 and 1 MW, with the operating cavity modes of $TE_{41,12}$ and $TE_{49,18}$, respectively. In addition, these investigations comprise numerous numerical experiments using an SGB at the RF window output plane. Prior to the fabrication, the numerical realization ensures the efficient design of the MOU. This method provides a unique and innovative approach for estimating ellipticity and astigmatism crucial for optimizing the MOU design without a priori information of the experimental beam data at the exit of the window plane. This methodology, a highlight of the work, enables a simple yet accurate estimation of the MOU design. Our in-house code, Gyrotron Design Suite (GDS-2018) [25], is used for the design of NLT, RF window, MOU, and initial design parameters of QOLs. Further the QOLs are optimized using commercial code launcher optimization tool (LOT) [26]. GDS-2018 is also been utilized for IPRA and generating mirror profiles in the MOU in order to support the beam propagation from the RF window to the corrugated waveguide.

TABLE I

DESIGN PARAMETERS OF NLT FOR TWO 300-GHZ GYROTRONS WITH THE OUTPUT POWER LEVEL OF 0.5 MW ($TE_{41,12}$) AND 1 MW ($TE_{49,18}$)

Parameters	0.5 MW, $TE_{41,12}$ [10]	1 MW, $TE_{49,18}$ [11]
$L_1/L_2/L_3/L_3^{'}$ (mm)	14/12.5/12/35	14/12.5/14/37.8
$\theta_1/\theta_2/\theta_3$ (°)	2.5/0.0/2.5	2.5/0.0/2.5
R_0 (mm)	14.36	19.27
$R_{nlt}/R_{nlt}^{'}$ (mm)	14.88/15.36	19.88/20.62
Transmission Efficiency (%)	99.48	99.53

The rest of the article is organized as follows: in Section II, the NLT design studies for both structures, 0.5 MW, $TE_{41,12}$ and 1 MW, $TE_{49,18}$, are carried out. In Section III, a detailed design approach for the QOLs is carried out in order to achieve an output beam with GCF >98%. Section IV discusses the transmission and reflection coefficients of the RF window. In Section V, the MOU system is designed to support the beam propagation in corrugated waveguide by utilizing IPRA to reconstruct the phase and amplitude profiles of the output beam. Finally, in Section VI, conclusions are drawn.

II. DESIGN STUDIES OF NLT

The NLT is a transformer that connects the gyrotron interaction cavity to the oversized QOL. The gyrotron interaction cavity consists of straight middle section (L_2), input section with down-tapered (L_1), and output section with up-tapered (L_3). All the three sections are inter connected with the parabolic rounding (θ) of 2.5° to avoid mode conversion. Specifically, the gyrotron's output cavity radius (R_0) determines the NLT input radius (R_{nlt}), while the QOL input radius (R_{qol}) determines the NLT output radius (R'_{nlt}). The transmission efficiency of NLT should be greater than 99%, with negligible mode conversion. In this study, two distinct NLTs are designed for two different gyrotrons operating at 0.5 and 1 MW, respectively. For the 0.5 MW, $TE_{41,12}$ gyrotron, the NLT is designed with the parameters as tabulated in Table I, where the transmission efficiency is more than 99.48%. Further, the design study is carried out for the design of NLT to support the 1 MW, $TE_{49,18}$ gyrotron output system. Both the input and output radii are calculated as 19.88 and 20.62 mm (≈1.07 times of R_0), respectively. Fig. 1 shows the cross section of the NLT and the gyrotron interaction cavity to support 1 MW of output power. The complete structure of the NLT is designed using GDS-2018 [25]. As shown in Fig. 1, the gyrotron cavity is attached to the NLT, and the optimized length of the NLT (L'_3) is 37.8 mm and total length of the NLT including up-taper becomes 51.8 mm, whereas the transmission efficiency achieved is greater than 99.53%.

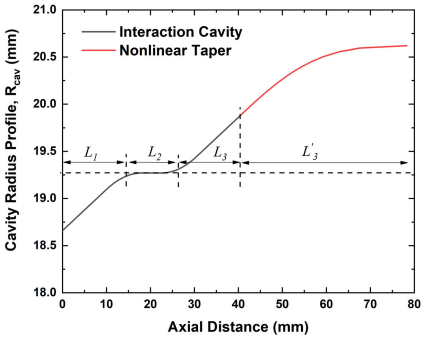

Fig. 1. NLT attached to the interaction cavity of the 300-GHz gyrotron operating at 1 MW, $TE_{49,18}$ mode.

III. QOL Design and Optimization

The QOL is an enlarged waveguide slot emitter with a mode converting perturbed inner surface that provides longitudinal and azimuthal beam focusing. It is connected to the interaction cavity of the gyrotron via an NLT section and plays a crucial role in safeguarding the gyrotron from harmful reflections, thereby ensuring optimal performance. The configuration employs NLT for a gradual transition of the RF wave to the launcher, thereby minimizing mode conversion. In high-power gyrotrons, the QOL converts the higher order cavity mode to the linearly polarized Gaussian-like mode TEM_{00}, which is essential for separating the high-power radiation from the electron beam using the QOL. A primary design objective for the QOL is to ensure that the output beam has a high Gaussian content factor (GCF) (>95%) while minimizing stray radiation losses (<3%) [13]. In designing of the launcher, achieving the desired output beam with high GCF and minimal stray radiation losses can be challenging. However, by incorporating surface perturbations in the wall, a QOL can generate the required GCF. In this work, the optimization of the launcher is conducted using the LOT to achieve a high Gaussian content factor [26]. To ensure a streamlined conversion to a Gaussian mode for tapered designs, various azimuthal variations are incorporated into the launcher's surface. The optimization process involves adjusting spline points to enhance the Gaussian content of the launcher. The calculation of waveguide fields is facilitated by coupled mode equations, while the radiation of the field in the aperture is determined through a Stratton–Chu diffraction integral. A detailed analysis of QOL is provided in [27] and [28]. In the current design, after the NLT section, the QOL mode converter section is designed with an oversize radius nearly 1.07 times of R_o. The oversize factor has a substantial effect on the fields within the launcher, necessitating cautious design optimization. Whereas, in order to achieve the required GCF at the desired frequency, the launcher section radius in this design is tapered to improve the GCF. Despite its advantages in minimizing unwanted oscillations and providing adequate clearance for the electron beam, the tapering method also results in an increase in diffraction loss and a reduction in beam quality. Hence, in designing of QOL for higher order modes at extremely high frequency, it is crucial to maintain a tradeoff between the Gaussian content of the outgoing wave beam and the launcher's compactness.

TABLE II
Design Parameters of QOL of 0.5 MW Output Power Gyrotron With $TE_{41,12}$ Mode and 1 MW Output Power Gyrotron With $TE_{49,18}$ Mode

Parameters	0.5 MW, $TE_{41,12}$	1 MW, $TE_{49,18}$
Launcher Length (mm)	179	179
Helical Cut Length (mm)	32.22	42.27
Launcher Radius (mm)	15.36	20.62
Taper Angle (Rad.)	0.003	0.004
Gaussian Content Factor (%)	99.32	98.58
Energy Conversion Efficiency (%)	99.13	97.80

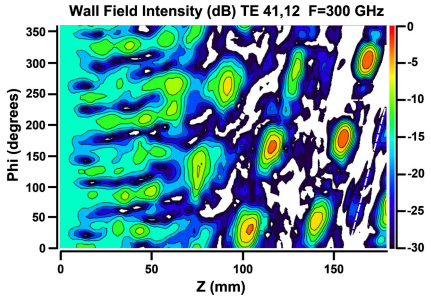

Fig. 2. Wall field intensity on the launcher's open-cut length section of 0.5 MW, $TE_{41,12}$ gyrotron obtained using LOT [26].

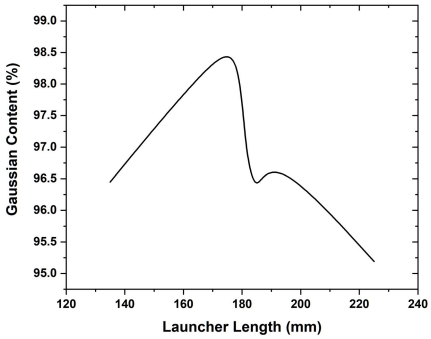

Fig. 3. Parametric analyses of the launcher length against GCF for the 1 MW gyrotron, operating at 300 GHz, $TE_{49,18}$ mode.

This study includes two separate QOL design studies for gyrotrons operating at 0.5 and 1 MW, respectively. Firstly, the design studies of QOL for the 0.5 MW gyrotron, operating at the mode $TE_{41,12}$ [10], were carried out, where the launcher radius is 15.36 mm with an oversize factor of 1.07, and wall surface deformations incorporate surface perturbations. To obtain a high Gaussian content at the desired frequency, a tapered launcher with 0.003 rad and a launcher cut length of 32.22 mm are employed. The launcher length is extended to 179 mm and 99.32% GCF with 99.13% energy conversion efficiency is obtained with this design. Fig. 2 presents the wall field intensity on the launcher's open-cut length section.

Further, the design studies of QOL for the 1 MW gyrotron, operating at 300 GHz, $TE_{49,18}$ mode, are carried out. The parametric calculations are performed to obtain the GCF nearly 98.58% with 97.80% energy conversion efficiency, where the launcher radius is 20.62 mm, launcher cut length is 42.27 mm with an oversize factor of 1.07. The GCF varies with launcher length, as seen in Fig. 3, with 179 mm of launcher length providing good agreement with the GCF.

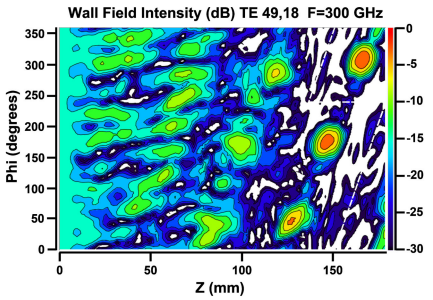

Fig. 4. Wall field intensity on the launcher's open-cut length section of 1 MW, $TE_{49,18}$ gyrotron obtained using LOT [26].

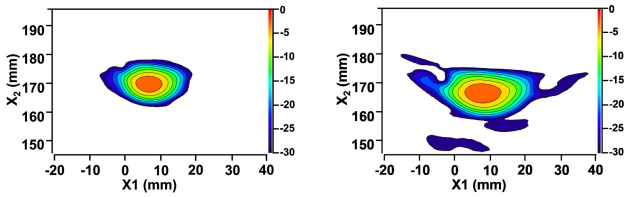

(a) (b)

Fig. 5. Planar field intensity plots for (a) 0.5 MW, $TE_{41,12}$ and (b) 1 MW, $TE_{49,18}$ at the open cut of the launcher at distances of 15.36 and 20.62 mm from the cavity center obtained using LOT.

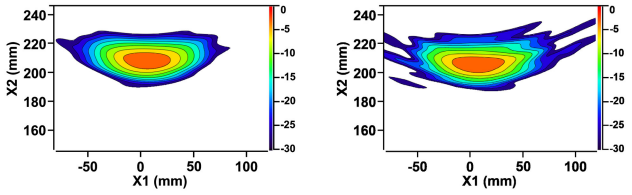

(a) (b)

Fig. 6. Planar field intensity obtained using LOT at a plane situated 80 mm away from the open-cut section of the launcher for (a) 0.5 MW, $TE_{41,12}$ and (b) 1 MW, $TE_{49,18}$.

Hence, the launcher's performance is improved by optimizing the taper angle 0.004 rad, overall launcher length 179 mm, and helical-cut length 42.27 mm. Table II comprises the design parameters and output mode content. The wall field intensity graph is shown in Fig. 4. The launcher's output beams are found to be down-converted to a Gaussian-like mode. In contrast, the field intensity is lowest near the white dashed line (cut edge) as shown in Figs. 2 and 4.

Further, Fig. 5 shows the planar field intensity plots for 0.5 MW, $TE_{41,12}$ and 1 MW, $TE_{49,18}$ at the open cut of the launcher. The open cut is positioned at distances of 15.36 and 20.62 mm, respectively, from the center of the cavity. For the 0.5 MW gyrotron output system, the Gaussian beam dimple dimensions at the launcher cut are $w_x = 23\lambda$ and $w_y = 16\lambda$. Whereas, for the 1 MW gyrotron output system, the Gaussian beam dimensions measure $w_x = 24\lambda$ and $w_y = 17\lambda$. Here w_x and w_y represent the dimple waist at x and y axis, respectively. Fig. 6 presents the planar field intensity at a plane situated 80 mm away from the open-cut section of the launcher. This distance exceeds twice the launcher radius and is a potential location for positioning the first mirror. In the QOL optimization process, the launcher's far-field ($>2D^2/\lambda$) pattern is analyzed and shaped into a Gaussian

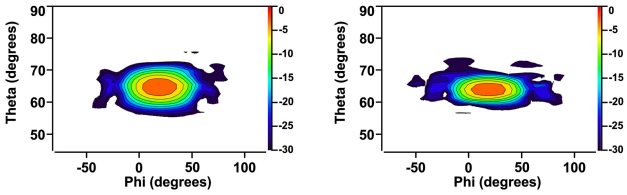

(a) (b)

Fig. 7. Far-field intensity obtained using LOT for (a) 0.5 MW, $TE_{41,12}$ and (b) 1 MW, $TE_{49,18}$.

TABLE III

DESIGN PARAMETERS AND RESULTS OF A SINGLE-DISK WINDOW FOR THE HIGH-POWER EXTRACTION FROM 300-GHZ GYROTRON

Parameters	Values
Window Material	CVD Diamond
Window Aperture Radius (mm)	50
Disk Thickness (mm)	1.89 mm
Disk Dielectric Constant	5.67
Transmission Coefficient (%)	99.92
Transmission Bandwidth (GHz)	2

distribution. Subsequently, the GCF is computed to quantify the proportion of power within the launcher beam aligned with the fundamental Gaussian mode, indicating efficient and focused energy transfer. Fig. 7 displays the far-field intensity plot, demonstrating Gaussian nature in the far-field region. The GCF for the far-field pattern in Fig. 7 is 99.16% for the 0.5 MW gyrotron with $TE_{41,12}$ mode, and 96.42% for the 1 MW gyrotron with $TE_{49,18}$ mode. From these plots, it is evident that the down-converted beams (from $TE_{41,12}$ and $TE_{49,18}$ mode to Gaussian-like TEM_{00} mode) are clearly emerging from the helical cut in both cases without significant losses.

IV. SINGLE-DISK CVD DIAMOND RF WINDOW

Gyrotrons rely on RF window to extract the high-power output beam, which separates the vacuum inside the gyrotron from the outer transmission line. These RF windows require materials with low loss tangent and high mechanical and thermal strengths. One popular choice for megawatt-class gyrotrons is the chemically vapor deposited (CVD) diamond window, which is a commonly used material for RF window in megawatt-class gyrotrons due to its low loss tangent, high mechanical and thermal strength, and ability to handle high power levels. The present design employs a common single-disk CVD diamond window with thickness of 1.89 mm ($9\lambda/2$) and an aperture radius of 50 mm for gyrotrons with 0.5 MW ($TE_{41,12}$) and 1 MW ($TE_{49,18}$) output power. The dielectric property of the window material is a crucial factor in the design of RF window with high power-handling capacity, as they influence both power absorption and transmission [1]. For the present study, the CVD diamond with a permittivity of 5.67 enables both gyrotrons operating with higher transmission and lower reflection at 300 GHz. The design of RF window is carried out using GDS-2018 [25], whereas the design parameters and the results are listed in Table III. The transmission and reflection coefficients of the window at various frequencies

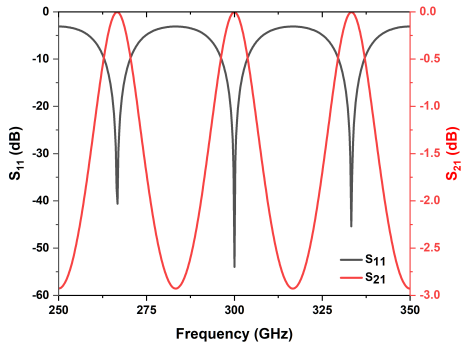

Fig. 8. Transmission (S_{21}) and reflection (S_{11}) coefficients of the RF window with 1.89 mm disk thickness at various frequencies between 250 and 350 GHz obtained using GDS-2018 [25].

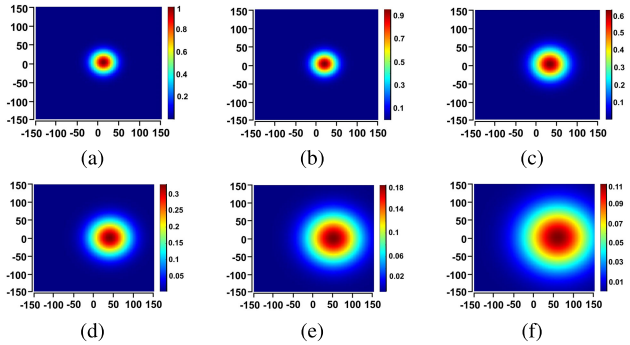

Fig. 9. Field intensity divergence and off-axis incidence from the centroid position of the SGB are plotted at various distances from the RF window section, with profiles at (a) 0, (b) 80, (c) 350, (d) 500, (e) 750, and (f) 1000 mm, obtained using GDS-2018 [25].

between 250 and 350 GHz regime are shown in Fig. 8. The designed window has a transmission bandwidth of 2 GHz (at -20 dB) and a transmission coefficient of approximately 99.92% for the output beam traveling through the window at the operating frequency of 300 GHz.

V. Design Studies of MOU

In the design studies of the MOU, common mirror profiles featuring two beam-shaping mirrors, denoted as mirror-1 (M1) and mirror-2 (M2) (as shown in Fig. 13), are analyzed after the RF window for 300-GHz gyrotrons, each operated at distinct output power levels, specifically 0.5 and 1 MW. However, the analysis of an internal mirror system after the QOL is not included in this work. Therefore, for a realistic beam intensity assumption, an SGB is introduced, which exhibits intensity divergence and off-axis incidence with distance, significantly enhances the overall realism of the design studies. The MOU, equipped with two beam-shaping mirrors, is strategically designed to ensure the efficient coupling of the output beam from the RF window to the corrugated waveguide while preserving beam ellipticity. The diameter of the corrugated waveguide plays a crucial role in determining the spacing between these mirrors. To address the space constraints between the mirrors, curvature is introduced to the M1 surface. Consequently, the precise positioning and optimization of the mirror system are required to maintain the Gaussian profile of the output beam by correcting both ellipticity and astigmatism. A corrugated waveguide system is used for the Gaussian beam transport from the gyrotron to the core of the tokamak. The diameter of the corrugated waveguide is considered as 63.5 mm (widely considered dimension in fusion tokamaks) [8]. The desired beam waist (w_x) along the x-direction and (w_y) along the y-direction at the input of the corrugated waveguide is determined as 20.32 mm (0.32 $\times$ diameter). Fig. 9 shows that the beam radius of the SGB (with beam waist 20.2 $\times$ 20.32 mm) increases over the distance. The distances w_x and w_y change to 21.1 and 19.4 mm as shown in Fig. 9(b). In addition, to account for more realistic conditions, the beam intensity's centroid position, initially kept 2.5 mm off-axis from the center [Fig. 9(a)], shifts to 15 mm off-axis with distance [Fig. 9(f)]. As the corrugated waveguide is usually located away from the RF window, it is crucial to maintain the beam waist and centroid position as the beam propagates in the free space.

A. Reconstruction of Precise Beam Intensity and Phase Computations

Accurate mirror surface profiling demands understanding of the phase at that particular plane. Phase mismatch is not a significant concern for certain low-power operations, but during high-power operations, any mismatch may cause an attributable power loss. As a result, precise beam intensity and phase computations are necessary. In addition to conventional methodologies, theoretical phase retrieval methods must be used to acquire the phase at extremely high power levels. The IPRA and the irradiance moment method are two standard ways of estimating the phase at different planes after the RF window. The IPRA is used in this study because of its improved near-field computation accuracy and capacity to minimize modulation effects in the propagating field. A method developed initially for phase reconstruction from two intensity measurements [21] is used to obtain phases from several measured or simulated intensity planes. Fig. 10 illustrates the two-plane technique in detail where plane-1 and plane-2 are denoted as z_1 and z_2, respectively. First, a random phase (φ_1) assumption for z_1 is used to multiply with the simulated or measured intensity A_1. In this work, the GDS-2018 is used to simulate the Gaussian beam intensity profiles of these planes [25]. A Huygens–Fresnel propagator is used to send the resulting beam along z_2 ($\tilde{A}_2, \tilde{\varphi}_2$) in a forward direction [14]. The Huygens–Fresnel propagator can be expressed as

$$h_{i\to j}(x, y) = \frac{1}{i\lambda\Delta z}\exp\left\{i2\pi\frac{\Delta z}{\lambda}\right\}\exp\left\{i\pi\frac{x^2+y^2}{\lambda\Delta z}\right\} \quad (1)$$

where, $k = 2\pi/\lambda$ and $\Delta z = (z_j - z_i)$. The electromagnetic field at the ith plane can be expressed as

$$f_i(x, y) = A_i(x, y)exp\left[i\varphi_i(x, y)\right] \quad (2)$$

where the ith plane wave amplitude and phase are denoted as $A_i(x, y)$ and $\varphi_i(x, y)$, respectively. Whereas electromagnetic field at the jth plane at a distance of z_{ij} can be expressed as

$$f_j(x, y) = F^{-1}\left\{exp\left[i\left(z_j - z_i\right)k_z\right] \times F\left[f_i(x, y)\right]\right\} \quad (3)$$

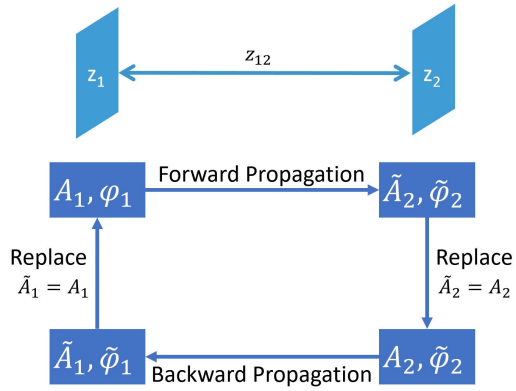

Fig. 10. Two-plane illustrates the IPRA technique where plane 1 and plane 2 are denoted as z_1 and z_2 whereas, in z_1 plane, the phase and amplitude of the incident beam are denoted as φ_1 and A_1, respectively.

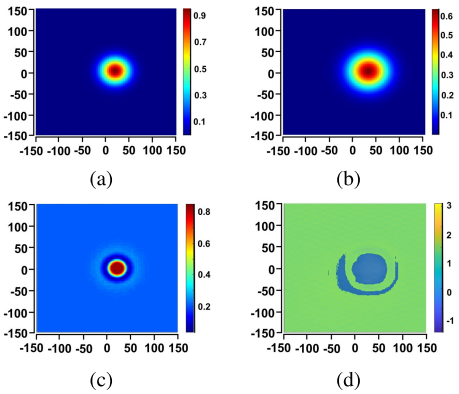

Fig. 11. (a) SGB contour at z_1, (b) SGB contour at z_2, (c) reconstructed SGB contour at z_2, and (d) retrieved phase, obtained using GDS-2018.

where F and F^{-1} represent the Fourier transform and its inverse [14], [22].

In the next step, replace the computed amplitude at z_2 ($\tilde{A}_2$) with the simulated or measured intensity at that plane (A_2). Using the same propagator used for z_2, the modified beam at z_2 is sent back to z_1 and its intensity ($\tilde{A}_1$) is replaced with the measured or simulated amplitude (A_1) at z_1. The steps above are repeated until the reconstruction efficiency reaches a certain threshold.

In this work, the amplitude contour and the phase reconstruction are carried out using GDS-2018 and the process is based on simulated amplitude contours obtained using SGB at the plane separated by 80 mm from the RF window plane. The plane separation between the known amplitude plane and the reference plane is calculated using $z_i = M(\Delta x)^2/\lambda$, where Δx is the mesh size, and M is sampling points. For the present study, z_i is calculated as 270 mm for both the design, that is, 0.5 MW, $TE_{41,12}$ and 1 MW, $TE_{49,18}$, whereas the amplitude contour intensity plane dimension is taken as 300×300 pixels with $M = 256$. The intensity of the SGB and the reconstructed intensity are shown in Fig. 11, and the effectiveness of the reconstruction in terms of the number of iterations is shown in Fig. 12. These results illustrate the efficacy of IPRA.

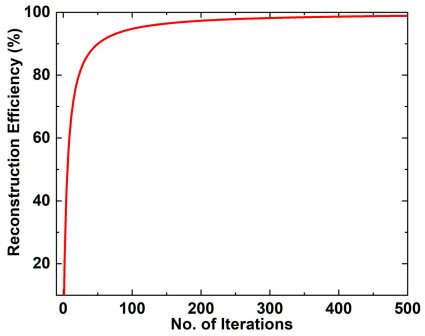

Fig. 12. Effectiveness of the reconstruction in terms of the number of iterations obtained using GDS-2018.

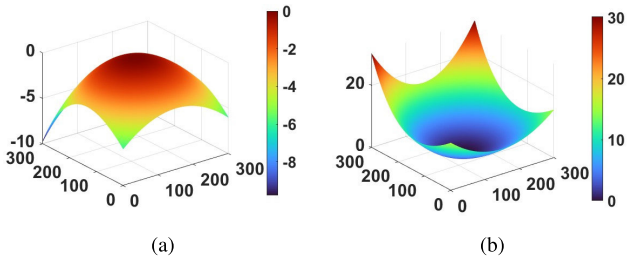

Fig. 13. Optimized external mirrors profile after the RF window for the conventional cavity gyrotrons of 0.5 and 1 MW output power with (a) mirror-1 and (b) mirror-2, obtained using GDS-2018.

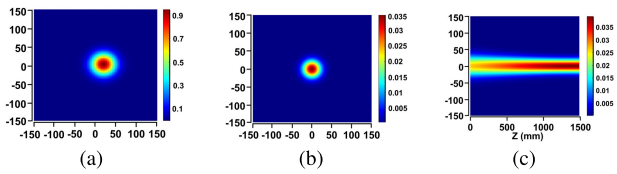

Fig. 14. Field intensity plot shows (a) incident SGB field intensity on M1 at 80 mm from the RF window, (b) output beam intensity after converging the beam intensity with the MOU system after 350 mm with reduced off-axis incidence, and (c) side view of the propagating waves obtained with GDS-2018.

B. Mirror Profile Optimization

The MOU system is IPRA-based and comprises two beam-shaping mirrors utilized to rectify the off-axis incidence of the Gaussian beam. For the design of common mirror profiles for conventional cavity gyrotrons with two distinct output power levels, namely 0.5 and 1 MW, GDS-2018 [25] is employed. As depicted in Fig. 13, the common mirror profiles exhibit two beam-shaping mirrors, forming an external mirror system, positioned after the RF window. To mitigate beam intensity divergence and minimize off-axis incidence, an SGB intensity at a distance of 80 mm from the RF window is applied to M1. Furthermore, M2 is situated at 350 mm, separated by 270 mm from M1, and oriented at a 45° angle with respect to the incident beam. This arrangement is optimized to maintain beam ellipticity (∼1) and reduce incident beam astigmatism ($\Delta z_0 \backsimeq 0$). Fig. 14(a) shows the incident SGB intensity on M1, where the beam-waist position is 7.5 and 0 mm along x-direction (z_x) and y-direction (z_y), respectively; Fig. 14(b) depicts the corrected beam intensity where w_x is 20.32 mm and w_y is 20.32 mm, whereas, Fig. 14(c) shows the side view of the propagating waves up

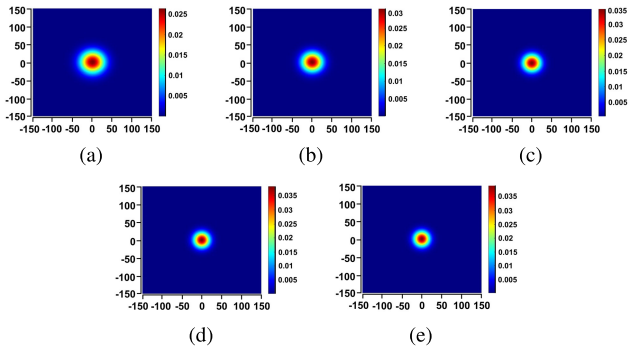

Fig. 15. Field intensity convergence and minimized off-axis incidence of the SGB are plotted at various distances inside the MOU, with profiles at (a) 80, (b) 350, (c) 500, (d) 750, and (e) 1000 mm, obtained using GDS-2018.

TABLE IV
BEAM PARAMETERS BEFORE AND AFTER THE MIRROR OPTIMIZATION

Parameters	Incident Beam	Output Beam	Desired
w_x (mm)	21.1	20.32	20.32
w_y (mm)	19.4	20.32	20.32
z_x (mm)	7.5	1.5	0
z_y (mm)	0	0	0
Ellipticity	1.08	1	1
Gaussian Mode Purity (%)	98.32	98.88	100
Astigmatism (Δz_0) (mm)	7.5	1.5	0

to 1500 mm. Notably, Δz_0 of the output beam intensity is reduced from 7.5 to 1.5 mm and the ellipticity is reduced from 1.08 to 1. Fig. 15 demonstrates the converged beam intensity with minimized off-axis incidence, where Fig. 15(c) shows the desired beam intensity 20.32 mm is reconstructed with minimized off-axis incidence of 1.5 mm along z_x after M2 positioned at 350 mm, and it remains unchanged up to 1500 mm, as shown in Fig. 14(c). Table IV provides specifications for the beam parameters associated with the incident and output beam intensities. Therefore, the modified beam intensity will enhance the coupling coefficient between the corrugated waveguide and the MOU for both gyrotrons.

VI. CONCLUSION

This study has conducted a comprehensive design analysis of complete output systems consisting of NLT, QOL, RF window, and MOU for two different gyrotrons with power levels of 0.5 and 1 MW. Two distinct designs of NLTs and QOLs have been considered for these gyrotrons, along with the common design of RF window and MOU. The optimization of the NLT using the GDS-2018 has resulted in high transmission efficiencies of 99.48% for the 0.5 MW design and 99.53% for the 1 MW design. The dimpled wall QOL, optimized with the commercial code LOT, has achieved high GCF of 99.32% and 98.58% for the respective power levels. The design of a common single-disk RF window made of CVD for both the gyrotrons has offered a reliable interface between the vacuum inside the gyrotron and the outer transmission line. The application of the IPRA facilitated accurate wave phase and amplitude contour reconstruction. The MOU, with two beam-shaping mirrors, has coupled the SGB to the corrugated waveguide while correcting ellipticity to 1 and reducing astigmatism to 1.5 mm. These design studies have demonstrated the feasibility and potential of the proposed output system components of gyrotrons for the DEMO tokamak. The achieved high transmission efficiency, accurate wave reconstruction, and beam-shaping capabilities enhance gyrotron system performance.

ACKNOWLEDGMENT

The authors would like to thank Dr. Gaurav Singh Baghel, NIT Silchar, India, for providing technical support.

REFERENCES

[1] M. V. Kartikeyan, E. Borie, and M. Thumm, *Gyrotrons: High-Power Microwave and Millimeter Wave Technology*. Berlin, Germany: Springer-Verlag, 2004.

[2] M. K. A. Thumm, G. G. Denisov, K. Sakamoto, and M. Q. Tran, "High-power gyrotrons for electron cyclotron heating and current drive," *Nucl. Fusion*, vol. 59, no. 7, Jul. 2019, Art. no. 073001, doi: 10.1088/1741-4326/ab2005.

[3] M. Thumm, "State-of-the-art of high-power gyro-devices and free electron masers," *J. Infr., Millim., THz Waves*, vol. 41, no. 1, pp. 1–140, Jan. 2020, doi: 10.1007/s10762-019-00631-y.

[4] S. Sabchevski, M. Glyavin, S. Mitsudo, Y. Tatematsu, and T. Idehara, "Novel and emerging applications of the gyrotrons worldwide: Current status and prospects," *J. Infr., Millim., THz Waves*, vol. 42, no. 7, pp. 715–741, Jul. 2021, doi: 10.1007/s10762-021-00804-8.

[5] D. Wagner et al., "Status of the new multi-frequency ECRH system for ASDEX upgrade," *Nucl. Fusion*, vol. 48, no. 5, May 2008, Art. no. 054006, doi: 10.1088/0029-5515/48/5/054006.

[6] S. B. Korsholm et al., "Current fast ion collective Thomson scattering diagnostics at TEXTOR and ASDEX upgrade, and ITER plans (invited)," *Rev. Sci. Instrum.*, vol. 77, no. 10, Oct. 2006, Art. no. 10E514, doi: 10.1063/1.2217921.

[7] J. Jelonnek et al., "Design considerations for future DEMO gyrotrons: A review on related gyrotron activities within EUROfusion," *Fusion Eng. Des.*, vol. 123, pp. 241–246, Nov. 2017, doi: 10.1016/j.fusengdes.2017.01.047.

[8] G. Granucci et al., "Conceptual design of the EU DEMO EC-system: Main developments and R&D achievements," *Nucl. Fusion*, vol. 57, no. 11, Nov. 2017, Art. no. 116009, doi: 10.1088/1741-4326/aa7b15.

[9] M. Morozkin et al., "Development of the prototype of high power sub-THz gyrotron for advanced fusion power plant (DEMO)," in *Proc. EPJ Web Conf.*, vol. 195, 2018, p. 1008 doi: 10.1051/epjconf/201819501008.

[10] D. Mondal, S. Yuvaraj, M. Rawat, M. V. Kartikeyan, and M. K. A. Thumm, "Design studies on 0.3-THz, 0.5-MW conventional cavity gyrotron for plasma heating," in *Proc. 22nd Int. Vac. Electron. Conf. (IVEC)*, Apr. 2021, pp. 1–2, doi: 10.1109/IVEC51707.2021.9721929.

[11] D. Mondal, S. Yuvaraj, M. Rawat, M. K. A. Thumm, and M. V. Kartikeyan, "Realistic design studies on a 300-GHz, 1-MW, DEMO-class conventional-cavity gyrotron," *IEEE Trans. Electron Devices*, vol. 69, no. 3, pp. 1442–1450, Mar. 2022, doi: 10.1109/TED.2022.3146101.

[12] S. Yuvaraj, M. V. Kartikeyan, and M. K. Thumm, "Design studies of a 3-MW, multifrequency (170/204/236 GHz) DEMO class triangular corrugated coaxial cavity gyrotron," *IEEE Trans. Electron Devices*, vol. 66, no. 1, pp. 702–708, Jan. 2019, doi: 10.1109/TED.2018.2876870.

[13] S. Yuvaraj, S. Illy, and M. V. Kartikeyan, "Electron gun and output coupling system for a 220-/251.5-GHz, 2-MW triangular corrugated coaxial cavity gyrotron," *IEEE Trans. Electron Devices*, vol. 64, no. 12, pp. 5134–5140, Dec. 2017, doi: 10.1109/TED.2017.2764942.

[14] G. S. Baghel and M. V. Kartikeyan, "Output system of a 220-/247.5-/275-GHz, 1.0-MW, triple-frequency regime gyrotron," *IEEE Trans. Electron Devices*, vol. 65, no. 4, pp. 1558–1563, Apr. 2018, doi: 10.1109/TED.2018.2808380.

[15] R. K. Dhakad, G. S. Baghel, M. V. Kartikeyan, and M. K. Thumm, "Output system for a 170-GHz/1.5-MW continuous wave gyrotron operating in the $TE_{28,12}$mode," *IEEE Trans. Plasma Sci.*, vol. 43, no. 1, pp. 391–397, Jan. 2015, doi: 10.1109/TPS.2014.2368254.

[16] E. M. Choi, M. A. Shapiro, J. R. Sirigiri, and R. J. Temkin, "Calculation of radiation from a helically cut waveguide for a gyrotron mode converter in the quasi-optical approximation," *J. Infr., Millim., THz Waves*, vol. 30, no. 1, pp. 8–25, Jan. 2009, doi: 10.1007/s10762-008-9418-x.

[17] O. Prinz, A. Arnold, G. Gantenbein, Y.-H. Liu, M. Thumm, and D. Wagner, "Highly efficient quasi-optical mode converter for a multi-frequency high-power gyrotron," *IEEE Trans. Electron Devices*, vol. 56, no. 5, pp. 828–834, May 2009, doi: 10.1109/TED.2009.2015819.

[18] P. C. Kalaria et al., "RF behavior and launcher design for a fast frequency step-tunable 236 GHz gyrotron for DEMO," *Frequenz*, vol. 71, nos. 3–4, pp. 161–171, Jan. 2017, doi: 10.1515/freq-2016-0212.

[19] S. Ruess et al., "KIT coaxial gyrotron development: From ITER toward DEMO," *Int. J. Microw. Wireless Technol.*, vol. 10, nos. 5–6, pp. 547–555, Jun. 2018, doi: 10.1017/S1759078718000144.

[20] G. Aiello et al., "Large area diamond disk growth experiments and thermomechanical investigations for the broadband Brewster window in DEMO," *IEEE Trans. Electron Devices*, vol. 68, no. 9, pp. 4669–4674, Sep. 2021, doi: 10.1109/TED.2021.3088077.

[21] J. R. Fienup, "Phase retrieval algorithms: A comparison," *Appl. Opt.*, vol. 21, no. 15, pp. 2758–2769, Aug. 1982, doi: 10.1364/AO.21.002758.

[22] S. Jawla, J.-P. Hogge, and S. Alberti, "Theoretical investigation of iterative phase retrieval algorithm for quasi-optical millimeter-wave RF beams," *IEEE Trans. Plasma Sci.*, vol. 37, no. 3, pp. 403–413, Mar. 2009, doi: 10.1109/TPS.2008.2011273.

[23] R. Ikeda et al., "Multi-frequency, megawatt-power gyrotron to facilitate a wide range of operations at ITER," *Nucl. Fusion*, vol. 63, no. 6, Jun. 2023, Art. no. 066028, doi: 10.1088/1741-4326/accdeb.

[24] J. Jin, G. Gantenbein, J. Jelonnek, M. Thumm, and T. Rzesnicki, "A new method for synthesis of beam-shaping mirrors for off-axis incident Gaussian beams," *IEEE Trans. Plasma Sci.*, vol. 42, no. 5, pp. 1380–1384, May 2014, doi: 10.1109/TPS.2014.2310903.

[25] S. Yuvaraj, G. S. Baghel, S. Singh, and M. V. Kartikeyan, "Gyrotron design suite (GDS-2018)," Dept. Private Community, Indian Inst. Technol. Roorkee, Roorkee, India, Internal Rep., 2018.

[26] J. Neilson, "Surf3d and TOL: Computer codes for design and analysis of high-perfonnance QO launchers in gyrotrons," in *Proc. Infr. Millim. Waves, Conf. Dig. Joint 29th Int. Conf. 12th Int. Conf. THz Electron.*, Sep. 2004, pp. 667–668 doi: 10.1109/icimw.2004.1422267.

[27] J. M. Neilson, "Optimal synthesis of quasi-optical launchers for high-power gyrotrons," *IEEE Trans. Plasma Sci.*, vol. 34, no. 3, pp. 635–641, Jun. 2006, doi: 10.1109/TPS.2006.875755.

[28] M. Blank, K. Kreischer, and R. J. Temkin, "Theoretical and experimental investigation of a quasi-optical mode converter for a 110-GHz gyrotron," *IEEE Trans. Plasma Sci.*, vol. 24, no. 3, pp. 1058–1066, Jun. 1996, doi: 10.1109/27.533113.